Microscopic and macroscopic simulations for femtosecond-laser–matter interaction by cubic interpolated propagation method

Yoshiaki Kondoh, Takashi Yabe,* Jun Maehara, Takashi Nakamura, and Youichi Ogata
Department of Mechanical Engineering and Science, Tokyo Institute of Technology, 2-12-1 O-okayama, Meguro-ku, Tokyo, 152-8552, Japan
(Received 19 February 2003; published 31 December 2003)

We performed 1.5-dimensional simulation for the Fokker-Planck equation using the CIP (cubic-interpolated propagation/constrained interpolation profile) method to investigate femtosecond-laser heating and transport processes. We found that the heat flux in the solid part approaches the Spitzer-Härm theory on quite a short time scale $\omega_p t < 50$, and thus the subsequent evaporation process can be analyzed by classical thermal conduction. On the basis of this result, we performed a hydrodynamic simulation using the CIP method with classical thermal conduction in order to investigate the long time behavior of the evaporation process. The experimental ablation depth was replicated very well, showing that even femtosecond pulse laser processing can be satisfactorily described by classical heat conduction. Since the damage size is shown to be much larger than laser-spot size even in such an ultrashort-pulse experiment, we must use the fluence estimated by the damage size, which is twice as large as the laser spot, to correctly replicate the experiments.

DOI: 10.1103/PhysRevE.68.066408 PACS number(s): 52.38.−r, 52.65.Ff

I. INTRODUCTION

Recently, there has been a growing interest in femtosecond-picosecond short-pulse laser experiments [1,2]. In such experiments by femtosecond-pulse lasers, the ablation depth was 10–100 times larger than the skin depth which is on the order of nanometers. Furthermore, the ablation depth increases in accordance with laser intensity, and this implies that some energy transport must take place.

We have had no such simulation on how the energy is transported on very short time scales and how the ablation depth is related to the dynamics on the hydrodynamic level. The purpose of this paper is to clarify the mechanisms in previously reported experiments with the aid of microscopic [3] and macroscopic simulations using the cubic-interpolated propagation/constrained interpolation profile (CIP) method [4–8].

II. NUMERICAL TECHNIQUE FOR MICROSCOPIC SIMULATION

Particle codes have been intensively used for analyzing instabilities and laser-matter interaction processes because of the low computational cost and low memory requirements in multidimensional calculations. However, it has been rarely used for energy transport processes because of inaccuracy in the distribution function f except for a δf algorithm that combines particle codes with grid codes [9]. For example, the heat flux is calculated by $q=\int (mu^3/2) f(4\pi u^2) du$ and hence the integral kernel depends on u^5, therefore main contribution to this flux comes from electrons at $u \approx \sqrt{5} u_{th}$ for a Maxwell distribution $f=f_0 \exp(-u^2/2u_{th}^2)$, where u_{th} is the thermal velocity. Since $f/f_0=\exp(-5/2)=0.08$ at $u \approx \sqrt{5} u_{th}$ only a small number of particles contribute to this flux and thus the particle code fails to accurately calculate the transport process.

As an alternative to the particle method, one of the authors proposed to apply the CIP [4–6] method to advection process in six-dimensional phase space [3] written as

$$\frac{\partial f}{\partial t}+\left(\mathbf{u}\cdot\frac{\partial}{\partial \mathbf{x}}\right) f+\left(\frac{\mathbf{F}}{m}\cdot\frac{\partial}{\partial \mathbf{u}}\right) f=0, \tag{1}$$

where $\mathbf{F}$ is the force and m the mass. Since the CIP can describe the advection process accurately even with coarse grid, it enables us to directly solve six-dimensional phase space in an Eulerian grid system. Actually, Landau damping has been accurately calculated even with ten grids in the whole velocity space [3]. Furthermore, exact particle conservation is guaranteed. This numerical technique was used to investigate fast ignition for inertial confinement fusion [10].

In this paper, we shall extend this algorithm to the Fokker-Planck equation

$$\frac{\partial f}{\partial t}+\left(\mathbf{u}\cdot\frac{\partial}{\partial \mathbf{x}}\right) f+\left(\frac{\mathbf{F}}{m}\cdot\frac{\partial}{\partial \mathbf{u}}\right) f=\left(\frac{\partial f}{\partial t}\right)_{coll} \tag{2}$$

with

$$\left(\frac{\partial f}{\partial t}\right)_{coll}=-Y\left[\sum_{\mu}\frac{\partial}{\partial u_\mu} f\frac{\partial H}{\partial u_\mu}+\frac{1}{2}\sum_{\mu,\nu}\frac{\partial^2}{\partial u_\mu \partial u_\nu} f\frac{\partial G}{\partial u_\nu \partial u_\mu}\right],$$

where

$$Y=4\pi\left(\frac{Ze^2}{m}\right)^2 \ln\Lambda,$$

$$H(\mathbf{u})=\frac{M+m}{M}\int\frac{f_s(\mathbf{U})}{\mathbf{V}}d\mathbf{U}$$

*Electronic address: yabe@mech.titech.ac.jp

$$G(\mathbf{u}) = \int f_s(\mathbf{U})\mathbf{V}d\mathbf{U},$$

$\mathbf{x}=(x,y,z)$, $\mathbf{U}=(U_x,U_y,U_z)$, and $\mathbf{u}=(u_x,u_y,u_z)$ are the ion and electron velocity, respectively. $\mathbf{V}\equiv\mathbf{u}-\mathbf{U}$ is the relative velocity. $f_s(\mathbf{U})$ is the ion distribution function, and f in Eq. (2) is the electron distribution function. Here $G(\mathbf{U})$ and $H(\mathbf{U})$ are called the Rosenbluth potentials [11], Z the ion charge, e the electron charge, $\ln\Lambda$ the Coulomb logarithm, M the ion mass, and m the electron mass.

This equation is put into nondimensional form by introducing the normalizing quantities such as the inverse plasma frequency $w_p^{-1}=(m_e/4\pi e^2 n_0)^{1/2}$ for time, the Debye length $\lambda_D=(k_B T_0/4\pi e^2 n_0)^{1/2}$ for length scale, the electron thermal velocity $u_{th}=(k_B T_0/m_e)^{1/2}$ for velocity, and $E_0=(k_B T_0/e\lambda_D)$ for electric field. Then we finally get

$$\frac{\partial f}{\partial t}+\left(\mathbf{u}\cdot\frac{\partial}{\partial \mathbf{x}}\right)f-\left(\mathbf{E}\cdot\frac{\partial}{\partial \mathbf{u}}\right)f = -\sum_{\mu}\frac{\partial}{\partial u_\mu}(Af)+\frac{1}{2}\sum_{\mu,\nu}\frac{\partial^2}{\partial u_\mu \partial u_\nu}(Bf), \quad (2')$$

$$A=\frac{Yn_0}{\omega_p u_{th}^3}\frac{\partial H}{\partial u_\mu}, \quad B=\frac{Yn_0}{\omega_p u_{th}^3}\frac{\partial^2 G}{\partial u_\nu \partial u_\mu},$$

where all the variables are now normalized although we use the same notation, for example, $\mathbf{u}$ in Eq. (2′) corresponds to $\mathbf{u}/u_{th}$ in Eq. (2), and H and G in Eq. (2′) represent Hu_{th}/n_0 and $G/(n_0 u_{th})$ in Eq. (2).

Let us now describe the numerical technique briefly. The one-dimensional form of the advection equation is given by

$$\frac{\partial f}{\partial t}+u\frac{\partial f}{\partial x}=0 \quad (3)$$

and Eq. (1) is merely the six-dimensional extension of this equation. In addition, the Vlasov or the Fokker-Planck equation has an important feature in that the advection velocity in each direction does not depend on the variable in the same direction. For example, the advection speed u_x in x direction does not depend on x, and the advection speed E_x in velocity space does not depend on u_x in Eqs. (1) and (2). In such a situation, the CIP method which will be used here has an interesting feature that it guarantees exact mass conservation.

Before proceeding further, let us explain the one-dimensional CIP scheme. Although nature operates in an essentially continuous world, a discretization process is unavoidable in order to implement numerical simulations. The primary goal of any numerical algorithm will be to retrieve the lost information inside the grid cell between these digitized points. The CIP method proposed by one of the authors tries to construct a solution inside the grid cell close enough to this real solution of the given equation with some constraints. We here explain its strategy by using an advection equation (3).

When the velocity is constant, the solution of Eq. (3) represents the simple translational motion of a wave with velocity $\mathbf{u}$. The initial profile [solid line of Fig. 1(a)] moves as the dashed line in the continuous representation. At this time, the solution at the grid points is denoted by circles and is the same as the exact solution. However, if we eliminate the dashed line as shown in Fig. 1(b), then information concerning the profile inside the grid cell has been lost. So it is natural to have a profile like that shown by the solid line in Fig. 1(c). Thus, numerical diffusion arises when we construct the profile by linear interpolation even with the exact solution as shown in Fig. 1(c). This process is called the first-order upwind scheme. On the other hand, if we use a quadratic polynomial for interpolation, it suffers from overshoot. This process is the Lax-Wendroff scheme.

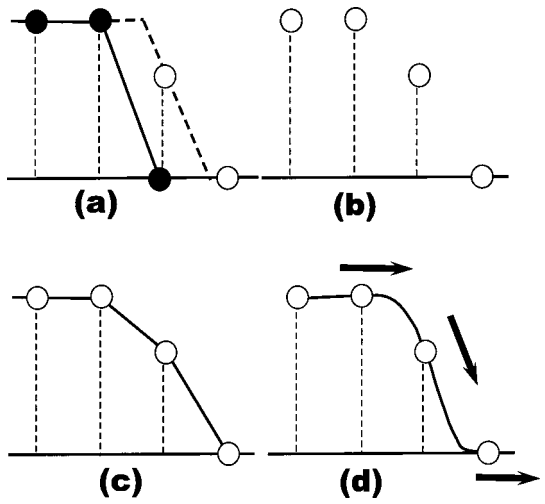

FIG. 1. The principle of the CIP method. (a) Solid line is initial profile and dashed line is an exact solution after advection, whose solution is (b) at discretized points. (c) When (b) is linearly interpolated, numerical diffusion appears. (d) In the CIP, spatial derivative also propagates and the profile inside a grid cell is retrieved.

What made this solution worse? The reason is we neglect the behavior of the solution inside grid cell and merely take care of the smoothness of the solution. From this point of view, we understand that a method incorporating the real solution into the profile within a grid cell is an important subject. We propose to approximate the profile as shown below. Let us differentiate Eq. (3) with spatial variable x, then we get

$$\frac{\partial g}{\partial t}+u\frac{\partial g}{\partial x}=-\frac{\partial u}{\partial x}g, \quad (4)$$

where g stands for the spatial derivative of f, $\partial f/\partial x$. In the simplest case where the velocity u is constant, Eq. (4) coincides with Eq. (3) and represents the propagation of the spatial derivative with a velocity u. By this equation, we can trace the time evolution of f and g on the basis of Eq. (3). If g is predicted after propagation as shown by the arrows in Fig. 1(d), the profile after one step is limited to a specific profile. It is easy to imagine that by this constraint, the solution becomes much closer to the initial profile which is the real solution. Most importantly, the solution thus created

gives a profile consistent with Eq. (3) even inside the grid cell. Importance of this constraint has been demonstrated in a previous paper [6].

If two values of f and g are given at two grid points, the profile between these points can be interpolated by a cubic polynomial

$$F_i(x)=a_iX^3+b_iX^2+g_iX+f_i, \tag{5}$$

where $X=x-x_i$. In order to extend the scheme to multidimensions later in this section, we introduce $\partial_x f\equiv\partial f/\partial x$ in the x direction and $\partial_y f\equiv\partial f/\partial y$ in the y direction instead of g. Thus, the profile at the $(n+1)$th step can be obtained shifting the profile by $u\Delta t$ as $f_i^{n+1}=F_i(x_i-u\Delta t), \partial_x f_i^{n+1}=dF_i(x_i-u\Delta t)/dx$:

$$f_i^{n+1}=a_i\xi^3+b_i\xi^2+\partial_x f_i^n\xi+f_i^n, \tag{6}$$

$$\partial_x f_i^{n+1}=3a_i\xi^2+2b_i\xi+\partial_x f_i^n, \tag{7}$$

where $\xi\equiv-u_i\Delta t$ and the superscript "n" indicates the time step. Thus the value and its derivative at the next time step $n+1$ are explicitly given. The coefficients a_i and b_i are determined so that the interpolation function and its first derivative coincide with the given value and derivative on the two grid points at step n,

$$F_i(x_i)=f_i^n, \quad (\partial F_i/\partial x)_{x=x_i}=\partial_x f_i^n,$$

$$F_i(x_{iup})=f_{iup}^n, \quad (\partial F_i/\partial x)_{x=x_{iup}}=\partial_x f_{iup}^n, \tag{8}$$

and this equation leads to

$$a_i=(\partial_x f_i^n+\partial_x f_{iup}^n)/\Delta x_i^2+2(f_i^n-f_{iup}^n)/\Delta x_i^3, \tag{9}$$

$$b_i=-(2\partial_x f_i^n+\partial_x f_{iup}^n)/\Delta x_i-3(f_i^n-f_{iup}^n)/\Delta x_i^2. \tag{10}$$

Here $\Delta x_i\equiv x_{iup}-x_i$ and $iup=i+\mathrm{sgn}(-u_i\Delta t)$, where $\mathrm{sgn}(w)$ means the sign of "w."

The CIP scheme can explicitly construct the cubic polynomial while the conventional spline method needs to use matrix solutions for interpolation. Mathematical analysis has shown that the CIP can produce an accurate solution even for a wavelength of two grid cells [6,12] with a computation time faster than the spline method or other higher-order schemes.

It is not economical to straightforwardly extend this technique to six dimensions because of the complexity of the six-dimensional cubic polynomial. Nakamura and Yabe [3] proposed a simple scheme to extend the CIP to six dimensions by employing a directional splitting technique. We shall briefly explain the strategy in the two-dimensional case:

$$\frac{\partial f}{\partial t}+u_x\frac{\partial f}{\partial x}+u_y\frac{\partial f}{\partial y}=0, \tag{11}$$

where u_x and u_y are the velocities in x and y directions, respectively. Instead of following the trajectory with the velocity (u_x,u_y), we shall use directional splitting as follows. At first, the movement with $(u_x,0)$ and then with $(0,u_y)$ are performed by

$$\tilde{f}_{ij}^n=L(x)f_{ij}^n, \tag{12}$$

$$f_{ij}^{n+1}=L(y)\tilde{f}_{ij}^n, \tag{13}$$

where $L(\lambda)$ is an operator of the one-dimensional CIP scheme which gives the solution of the equation

$$\frac{\partial f}{\partial t}+u_\lambda\frac{\partial f}{\partial\lambda}=0. \tag{14}$$

The solution of Eq. (12) is given by Eqs. (6) and (7) and Eq. (13) is also given by Eqs. (6) and (7) simply replacing x by y. In addition, the CIP method needs information on the spatial derivatives. Unfortunately, in calculating Eq. (13), the spatial derivative in the y direction, $\partial_y\tilde{f}_{ij}^n$, is unknown, because the solution of Eq. (12) gives only $\partial_x\tilde{f}_{ij}^n$ according to Eq. (7). Therefore, some method is required to estimate $\partial_y\tilde{f}_{ij}^n$ from $\partial_y f_{ij}^n$. Let us introduce an operator S to represent this procedure.

In order to clarify the procedure, we further introduce the operator $C(\lambda,\Delta t)$ which means the CIP solution of Eq. (14) is given by Eqs. (6) and (7) after the time interval Δt. Therefore the solution procedure in Eqs. (12) and (13) can be symbolically written as

$$\begin{pmatrix}\tilde{f}_{ij}^n\\ \partial_x\tilde{f}_{ij}^n\end{pmatrix}=C(x,\Delta t)\begin{pmatrix}f_{ij}^n\\ \partial_x f_{ij}^n\end{pmatrix}, \tag{15}$$

$$\partial_y\tilde{f}_{ij}^n=S(x,y,\Delta t)(\partial_x f_{ij}^n,\partial_y f_{ij}^n), \tag{16}$$

$$\begin{pmatrix}f_{ij}^{n+1}\\ \partial_y f_{ij}^{n+1}\end{pmatrix}=C(y,\Delta t)\begin{pmatrix}\tilde{f}_{ij}^n\\ \partial_y\tilde{f}_{ij}^n\end{pmatrix}, \tag{17}$$

$$\partial_x f_{ij}^{n+1}=S(y,x,\Delta t)(\partial_x\tilde{f}_{ij}^n,\partial_y\tilde{f}_{ij}^n). \tag{18}$$

The operator $S(\lambda,\beta,\Delta t)$ gives the solution of the equation

$$\frac{\partial}{\partial t}(\partial_\beta f)=-\frac{\partial}{\partial\beta}(u_\lambda\partial_\lambda f) \tag{19}$$

which is the spatial derivative of Eq. (14) in the β direction. Although the advection equation must be solved very accurately by the CIP method $C(\lambda,\Delta t)$, the evolution of the spatial derivative in other direction is not so important in such a process. Therefore we can adopt a lower-order finite difference scheme for this purpose. In the previous paper, we adopted the centered finite difference to Eq. (19). Then Eq. (16) is explicitly written as

$$\partial_y\tilde{f}_{ij}^n=\partial_y f_{ij}^n-\Delta t(u_{x,i,j+1}\partial_x f_{i,j+1}^n-u_{x,i,j-1}\partial_x f_{i,j-1}^n)/2\Delta y. \tag{20}$$

In the same way, Eq. (18) is given by

$$\partial_x f_{ij}^{n+1}=\partial_x\tilde{f}_{ij}^n-\Delta t(u_{y,i+1,j}\partial_y\tilde{f}_{i+1,j}^n-u_{y,i-1,j}\partial_y\tilde{f}_{i-1,j}^n)/2\Delta x. \tag{21}$$

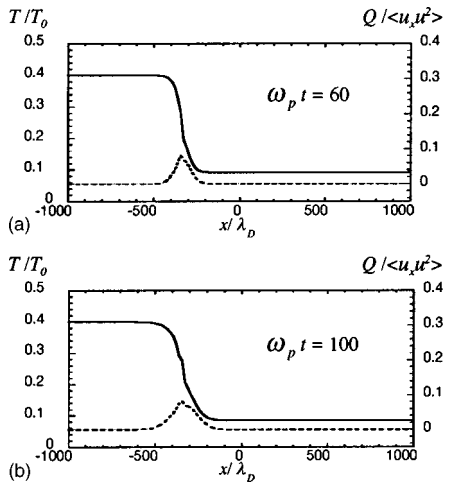

FIG. 2. (a) Temperature T and heat flow Q distribution at $\omega_p t = 60$, (b) 100.

This scheme has been proved to guarantee the exact conservation of particle number [3].

In applying this fractional step technique to the Fokker-Planck equation, we used the second-order splitting scheme as

$$f^*(\mathbf{x},\mathbf{u}) = f^n(\mathbf{x}-\mathbf{u}\Delta t/2,\mathbf{u}),$$

$$f^{**}(\mathbf{x},\mathbf{u}) = f^*(\mathbf{x},\mathbf{u}+\mathbf{E}\Delta t),$$

$$f^{n+1}(\mathbf{x},\mathbf{u}) = f^{**}(\mathbf{x}-\mathbf{u}\Delta t/2,\mathbf{u}).$$

III. NONLOCAL HEAT FLOW

Before applying the present scheme to the femtosecond-laser–matter interaction processes, we shall check the accuracy of the method by comparing it with the previous calculation for nonlocal heat flow [13]. In the previous paper, Bell *et al.* used the Fokker-Planck equation in one-space and two-velocity dimensions coupled with the Poisson equation.

Bell *et al.* numerically solved those equations by expanding f into Legendre polynomials in $\cos\theta$ up to eight terms. In the present calculation, however, we directly solve the equation in an Eulerian grid system.

We used a similar condition in which the plasma is initially uniform in density and temperature gradients are imposed. The system size is $2000\lambda_D$ described by 120 spatial grid points, where λ_D is the Debye length at n_0 and T_0. The velocity space is uniformly divided with 32 grids in the range $[-6.4u_{th}, 6.4u_{th}]$ in the u_x direction and 16 grids in the range $[-2.9u_{th}, 2.9u_{th}]$ in the u_y direction. Although we used such coarse grid points in velocity space, the previous paper [3] demonstrated the accuracy of the scheme even with such a grid.

The high temperature region is placed over 40 grid points on the left side with a temperature ($T = 0.4T_0$) four times larger than the low temperature layer ($T = 0.1T_0$), and these two layers are connected exponentially. Figure 2 shows the time evolution of the temperature and heat-flux distributions.

The temperature gradient spreads spatially and the heat flux reaches a maximum value at the boundary of the high temperature layer. Figure 3 shows the relation between the heat flux and the inverse temperature gradient normalized by the local collision mean free path $\lambda_{fre} \propto u_T^4/n$, where u_T and n are the thermal velocity and density at each local point, respectively. The circles correspond to the calculation result at $\omega_p t = 60$, and the squares at $\omega_p t = 100$.

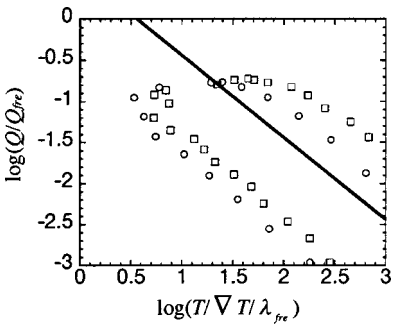

FIG. 3. Heat flux Q versus inverse temperature gradient at $\omega_p t = 60(\bigcirc), 100(\square)$. The vertical axis shows heat flux divided by free streaming limit, Q_{fre}. The scale length of temperature gradient is normalized by collision mean free path λ_{fre}.

This result is similar to that in Ref. [13]. The system size in Ref. [13] is $64 \times 34.71\lambda_D$ with a spatial grid size of $\Delta x/\lambda_D = 34.71$ and 32 velocity grids with a grid size of $\Delta u/u_{th} = 0.2$.

IV. FEMTOSECOND-LASER INTERACTION PROCESS

Since we confirmed that the present scheme can replicate the previous result on nonlocal heat flow, we shall now apply it to laser-matter interaction. Let us consider a system with a uniform-temperature region initially with a high-density layer placed on the left and a low-density layer on the right. The laser is assumed to be incident from the right and absorbed at the sharp transition layer. We limit the calculation to one-space dimension and two-velocity spaces.

The system size is $1000\lambda_D$ in the x direction. The high-density ($5n_0$) layer and the low-density ($0.5n_0$) plasma layer are connected exponentially with a layer of width $200\lambda_D$.

We assume that the initial electron distribution f_0 is Maxwellian, having uniform temperature $0.1T_0$. The number of numerical grid points is 120 in the x direction, 29 in the range $[-4u_{th}, 4u_{th}]$ in the u_x direction, and 17 in the range $[-4u_{th}, 4u_{th}]$ in the u_y direction.

The laser light represented by the electric field E_{ex} $[= E_0 \sin(\omega t), \omega = 0.5\omega_p]$ parallel to the x axis is imposed over the region $17\lambda_D$ from the critical surface of the plasma, whose density is $5/4n_0$, and exponentially decays in this region. We set the collision frequency at the thermal velocity u_{th} given by T_0 to be $\nu/\omega_p = 0.01$. [This corresponds to the parameters $n_0 = 10^{20}\ \mathrm{cm}^{-3}$ and $k_B T_0 = 1$ keV when the electron-ion collision frequency is estimated by $\nu = n_0 Y/u_{th}^3$ which appears in Eq. (2).] Since we set the initial temperature to be $0.1T_0$, collision frequency is initially $\nu_T/\omega_p \equiv n_0 Y/u_T^3\omega_p = 0.3$ if the thermal velocity u_T at this temperature is used.

The electric field is solved by coupling the Maxwell equation $\partial E/\partial t = J$ for the high-density region with the Poisson equation $\nabla \cdot \mathbf{E} = q$ for low-density region, where q is the charge. These two solutions are connected at the boundary near the critical point. Accelerated electrons ejected from the laser-heated region must be neutralized by some return current and therefore the Poisson equation is suitable for this area in order to accurately calculate the virtual cathode.

In the high-density layer, however, the motion becomes fluidlike in a time-averaged sense and, as a result, fluidlike motion becomes important there. Oscillations related to the Debye length are not important but the collision process is. If the plasma oscillation must be accurately solved in this region, the spatial grid size must be smaller than the Debye length and we will not be able to use a large system sufficient for resolving thermal transport. Therefore, Maxwell's equations used to calculate the electric field on average via macroscopic value are suitable in this area. For this reason, we solved electric field separately in the two regions by two methods. Therefore, the electric fields are connected as

$$E = E_{poi} \cdot (1 - e^{-1/n^2}) + E_{\max} \cdot e^{-1/n^2},$$

where E_{poi} represents the electric field solved by the Poisson equation $\nabla \cdot E_{poi} = q$ and E_{max} by the Maxwell equation $\partial E_{max}/\partial t = J$.

Figure 4 shows the electron motion in $x - u_x$ phase space at the time of (a) 50, (b) 75, and (c) 100 ω_p^{-1} after laser irradiation which lasted $4\pi\omega_p^{-1}$. Although we did not use particles for the calculation, we here employed virtual particles only for the purpose of visualization of the phase trajectories of the particles. These particles were initially placed at an arbitrary position in velocity space. Then we calculated how it moved under the influence of the calculated electric field with a leapfrog scheme by the equations

$$du_p(t)/dt = E(x_p(t), t), \tag{22}$$

$$dx_p(t)/dt = u_p(t), \tag{23}$$

where $E(x_p(t), t)$ is estimated at the particle location by linear interpolation from the values on the nearby grid points. The number of particles used here is 2040.

Figure 4 is only a part of the whole system. The negative velocity part of the electron distribution is moving towards the high-density side, while positive velocity part is moving towards the low-density side from the surface. In Fig. 4(a), the electrons in the heated region are accelerated and move out far away from the surface at the beginning. Next, electrons in the low-velocity region gradually perform circular motion near the heated surface. This is confirmed in Figs. 4(b) and 4(c), where particles initially having positive velocities changed their direction to negative velocity at $x = 0 \sim 20\lambda_D$. This structure is maintained up to the end of the calculation at $\omega_p t = 100$. Thus the electrons streaming into vacuum are reflected back to the high-density region by the virtual cathode formed there, and contribute to the heat flux in the high-density region.

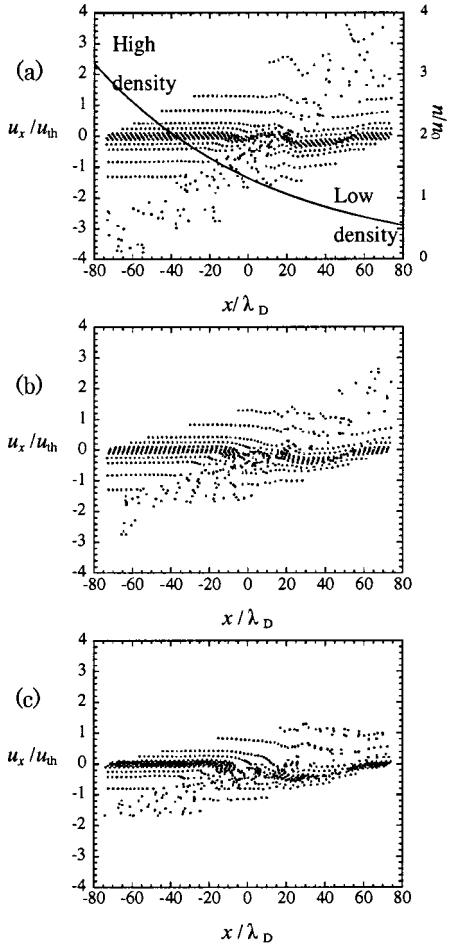

FIG. 4. Electron trajectories in $x - u_x$ phase space at $\omega_p t =$ (a) 50, (b) 75, and (c) 100. Density profile is shown by the solid line in (a) .

Open circles and the solid line in Figs. 5(a) and 5(b) show the temperature and heat-flux distributions at $\omega_p t = 50{,}100$, respectively. The relation between heat flux (normalized by the local free streaming flux $Q_{fre} = nv_T T$) and temperature gradient (normalized by the collision mean free path λ_{fre} estimated at each local point of x) at $\omega_p t = 50$ (c), 100 (d) are plotted in Fig. 5 and compared with the theoretical curve based on the Spitzer-Härm (S-H) theory $q = -\kappa \nabla T$ [14]. The calculated heat flux in the high-density region remains along the theoretical curve (solid line), whereas it departs seriously on the vacuum side.

Even at $\omega_p t = 50$ in Fig. 5(c), the flux in the high-density region already reached the S-H theory while it is not yet in steady state in the low-density region. It is important to note that such a classical Fourier law is quickly established. It is interesting to note that this behavior is different from the result in the preceding section. In such a nonlocal heat flow, the heat flux is always detached from the classical law as in Fig. 3. We have not yet come to a conclusion to explain this difference but the virtual cathode and returning electrons may play some role in establishing the classical Fourier law.

In order to show the effect of the virtual cathode, we performed another simulation in which self-consistent electric fields are not used to accelerate the electrons but only the

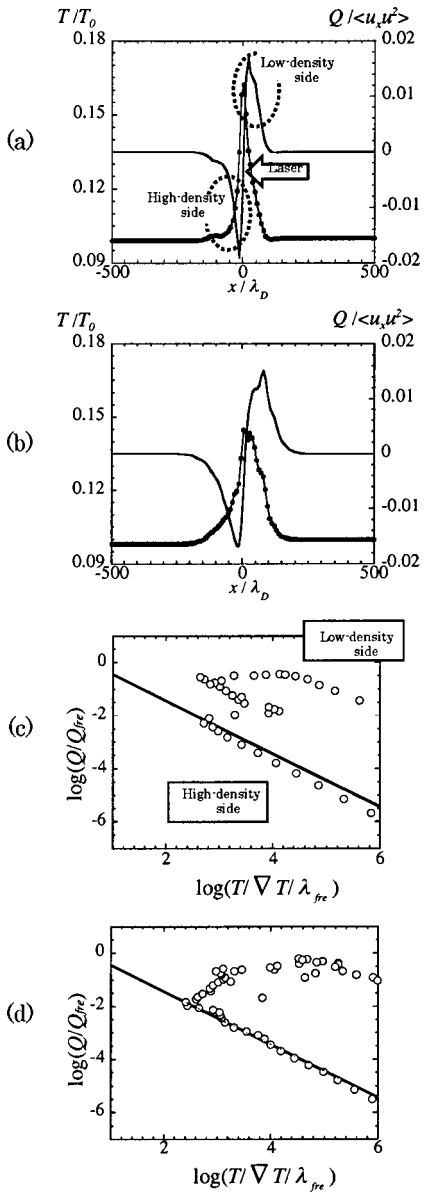

FIG. 5. Temperature (open circles) and heat-flux (solid line) distribution at $\omega_p t=$ (a) 50, (b) 100. Heat flux Q vs inverse temperature gradient at $\omega_p t=50$ (c), 100 (d). The theoretical curve based on the Spitzer-Härm theory is plotted by the solid line. Log base is 10.

laser field is imposed. Figure 6 shows the comparison of trajectories of electrons in $x-u_x$ phase space at $\omega_p t=50$ with and without self-consistent fields. Compared with Fig. 6(b), electrons in Fig. 6(a) are relatively confined in the region where the laser field was imposed because of the self-induced electric field. If this field is absent, a shocklike structure propagates with constant velocity in the entire velocity space of the electrons because electrons are moving with initially accelerated velocities.

Figure 7 shows the electric field distribution in the same case as in Fig. 6. The initial laser is imposed as $\mathbf{E}=E_0\sin(\omega t)$ (added in the region $x=0\sim-17$). The influence of the self-consistent electric field can be seen in Fig. 7(a). For $x>0$ there exists a region with $E>0$ which pulls

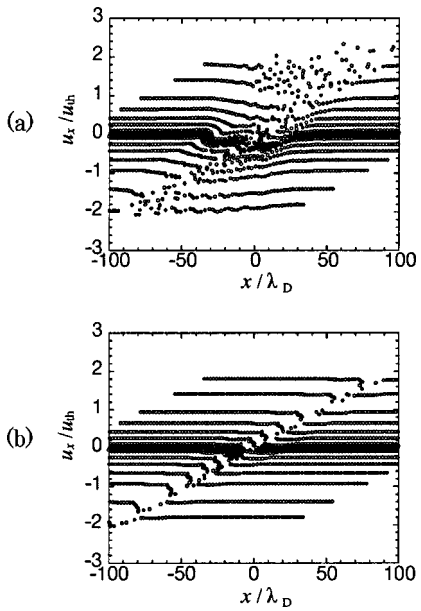

FIG. 6. Electron trajectories in $x-u_x$ phase space at $\omega_p t=50$, (a) with and (b) without the self-consistent fields.

back the electrons in the negative direction. This $\mathbf{E}>\mathbf{0}$ region should have acted as a virtual cathode. Figure 7(b) is the result without the self-consistent field but the electric fields are calculated from the resultant space charge. A very large electric field appeared because there is no self-consistent electric field to prevent charge separation.

Figure 8 shows the dependence of heat flux on the laser intensity $E_{ex}[=A\sin(\omega t)$, (a) $A=E_0/2$, (b) $A=E_0$, (c) $A=2E_0$, and (d) $A=3E_0]$. It is clear that the distance to which heat is transported becomes longer by increasing the laser intensity although the initially heated region is the

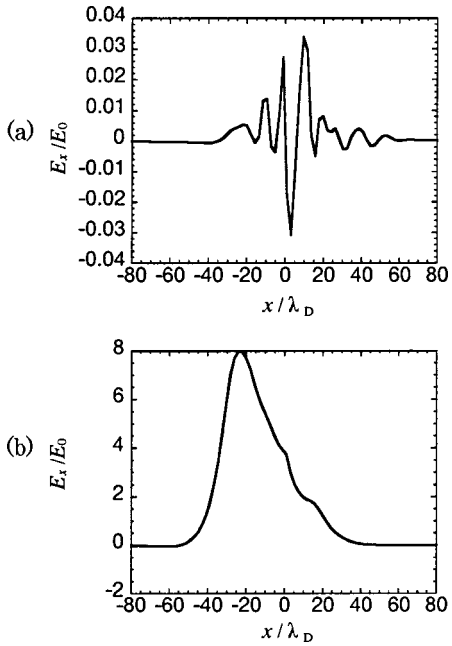

FIG. 7. Electric field distribution for the same condition as in Fig. 6 at $\omega_p t=50$ (a) with and (b) without self-consistent electric field.

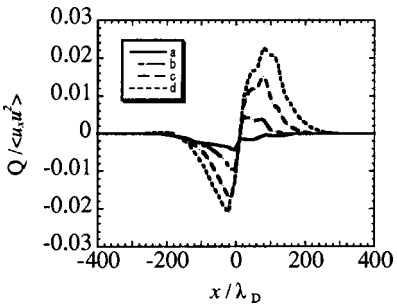

FIG. 8. The heat flux Q as functions of x at $\omega_p t=100$ for various laser field $E_{ex}[=A\sin(\omega t)$, (a) $A=E_0/2$, (b) $A=E_0$, (c) $A=2E_0$, and (d) $A=3E_0$].

same. This heat-penetration length is shown in Fig. 9 for various laser fields E_{ex}, where "d/λ_D" is the length which is estimated by the point where $Q=-4.15\times10^{-3}$ which corresponds to the edge of the initial electric field in the case of Fig. 8(a).

If this length is simply calculated from the distance that electrons would move with velocity gained from the laser field , the distance should be proportional to $\sqrt{A}$ but Fig. 9 shows somewhat different behavior.

Although the heat-penetration length increases with increasing laser intensity, this tendency does not explain the experimental results as will be shown later in the following section [1]. In order to explain the experimental results, we need a long time scale hydrodynamic simulations. The most important conclusion drawn from this microscopic simulation is that the classical heat conduction is established even at $\omega_p t\sim50$ which is very short compared with the laser pulse duration in the actual system. This proves that the classical thermal conduction through the electron-collision interaction takes place much earlier than expected.

Figure 10 summarizes the results with the various laser intensities. We added another calculation result with the spatial mesh size reduced by a factor of 4 for $A=E_0$. The system size is also reduced because the same number of meshes is used. The S-H theory is shown by the solid line for comparison. Because the denominator of heat flux in Fig. 10 is free-streaming flux $Q_{fre}(=nv_T T)$ estimated at each local position which becomes large in accordance with heat flux that also increases in proportion to $nv_T T$ when laser field is

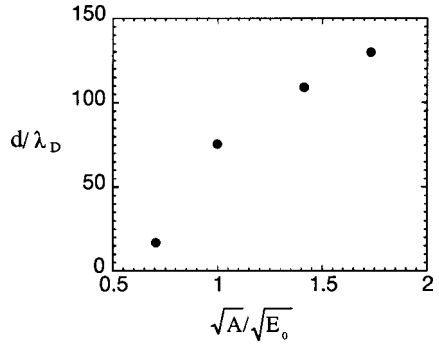

FIG. 9. Heat penetration depth vs incident laser field. This length is estimated by the point $Q=-4.15\times10^{-3}$.

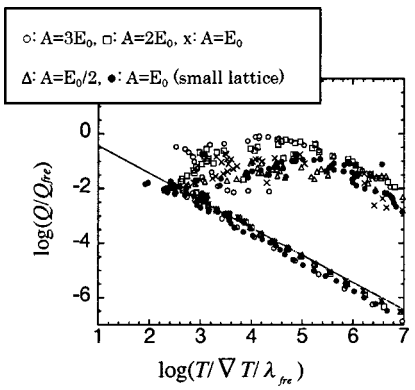

FIG. 10. The heat flux vs gradient scale for the various laser field at $\omega_p t=100$ ($A=E_0/2$, E_0, $2E_0$,) and $\omega_p t=50$ ($A=3E_0$). The calculation with fine mesh is added for $A=E_0$ in which spatial mesh size is reduced to 1/4, but the plot is at $\omega_p t=50$. The Spitzer-Härm theory is shown by the solid line.

increased. Therefore Q/Q_{fre} remains constant and shows unified behavior which does not depend on laser field. Moreover, the calculation with reduced mesh size also agrees with the coarse mesh result and this confirms the accuracy of the present calculations.

V. MACROSCOPIC SIMULATION

From the results by microscopic simulations in the preceding section, the classical thermal conduction is shown to be quickly established. However, the calculation in the preceding section is not long enough to compare the ablation depth with the experiments. Thus we need a simulation with a much longer time scale. Fortunately, we know at present that the classical thermal conduction is relevant for further simulation and hence we are able to perform the purely classical fluid dynamic simulation without any anomalies.

For this hydrodynamic simulation, we use the code PARCIPHAL based on the CIP method applied to hydrodynamic equations. This code has been used for various types of laser processing on time scales of nanoseconds-milliseconds and has demonstrated its suitability in such calculations [6,15–17]. This code includes thermal conduction, viscosity, the equation of state, elastic-plastic processes, surface tension, and other physics.

At first, the simulation is applied to copper with a laser pulse of 150 fs and a wavelength of 780 nm by setting the absorption rate to 30%. The laser pulse intensity is set to a Gaussian distribution in both space and time:

$$I=I_0\exp\left[-\left(\frac{r}{a}\right)^2\right]\exp\left[-\left(\frac{t}{\tau}\right)^2\right],$$

where I_0 is the peak value of the laser intensity. The penetration of the laser is given by the skin depth as

$$l_m=\frac{1}{4\pi}\sqrt{\frac{\lambda c}{\sigma}},$$

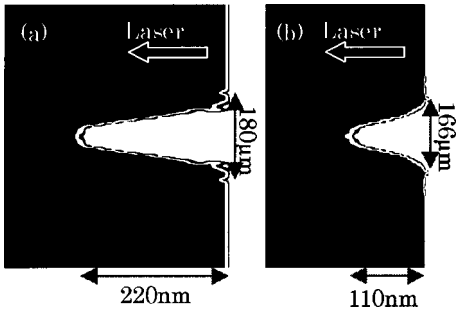

FIG. 11. The crater structure obtained by fluid simulation at 10 ns after laser irradiation. In the simulation, the laser spot diameter is 80 μm and laser energy is (a) 754 μJ, (b) 251 μJ. (The size of height and width in these figures is changed by $1:1.334\times10^3$ for better visualization.)

where λ is the laser wave length, c the speed of light, and σ the electric conductivity. Therefore, the depth l_m is about 5 nm for copper and is negligibly small compared with the crater depth observed in experiments.

Figure 11 shows two examples of crater shapes given by the hydrodynamic simulation. The laser enters from the right-hand side of the figure and irradiates the copper surface placed on the left-hand side. The laser energy in Fig. 11 is (a) 754 μJ and (b) 251 μJ with the same laser-spot diameter 80 μm. In Fig. 11, the depth and diameter of the craters (the ratio between the spatial scale height and width in the figure is changed to $1:1.344\times10^3$ in order to clearly show the crater depth) are about (a) 220 nm and 180 μm, and (b) 110 nm and 166 μm, respectively, 10 ns after laser irradiation. The crater stopped developing at this time. It is important to measure the size of the damaged area on the target surface, because the size of the damaged area is used as a spot size to estimate the laser fluence in the two experiments given in Figs. 13 and 14 [2,18].

We have performed a number of simulations by changing the fluence and spot size. Figure 12 shows the damage size for various laser-spot sizes and thus the damage size is always much larger than the laser-spot size. The error bar represents the change caused by different fluence or laser energy with the same spot size. Although the damage size has been widely believed to be the same as the laser-spot size under such an ultrashort-pulse laser, both differ significantly as shown in the figure. In the case of a laser-spot diameter of 80 μm, for example, the damage size on the target surface is 150–180 μm which is twice as large as the laser-spot size. Therefore we must be careful in analyzing the experimental results if the fluence is estimated by the damage size as in the experiments of Refs. [2,18,19].

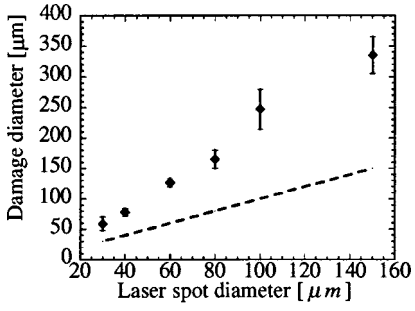

FIG. 12. Calculation results of damage diameter for various laser spot diameter, where the fluence is changed from 113 to 4 266 mJ/cm^2. The error bar indicates the change for different fluence. For comparison, the dashed line, which represents the damage size equal to the laser spot, is drawn.

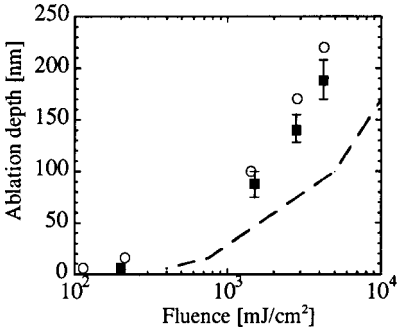

FIG. 13. Ablation depth vs fluence. The open circles show the simulation results with 80 μm laser-spot diameter for laser energy from 20 μJ to 754 μJ but the fluence was estimated by the damage size in Fig. 12, while the dashed line is the simulation result estimated by laser-spot size. The squares with error bar are the experimental results [2].

In Fig. 13, ablation depth is plotted against the laser fluence. The open circles are simulation results in which the laser-spot diameter is fixed to 80 μm but the fluence is estimated by the damage size for each simulation. The squares are the experimental results and the dashed line is the simulation result in which the fluence is estimated merely by the laser-spot size. As is expected from Fig. 12, a large difference appears depending on the definition of the fluence. As in Fig. 13, the hydrodynamic simulation with purely classical thermal conduction and elastic processes can replicate the experimental results very well when the fluence is correctly estimated in the same way as the experiments.

These results can also be confirmed by another similar experiment shown in Fig. 14 [18]. The simulation is for silver with a 120-fs laser pulse and a wavelength of 780 nm by setting the absorption rate to 10%. If we correctly estimate the fluence in the same way as in Fig. 13, the simulation agrees well with the experiment [18].

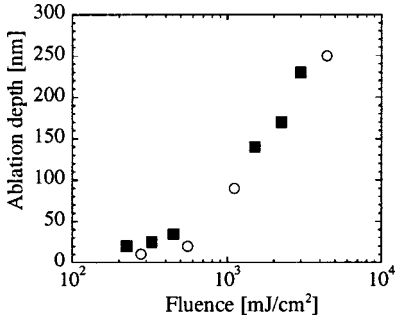

FIG. 14. Ablation depth vs effective fluence. The circles show the simulation results with 60-μm laser-spot diameter for laser energy from 31.4 μJ to 502.6 μJ but the fluence was estimated by the damage size. The squares represent the experimental results [16].

VI. SUMMARY

We performed simulations to analyze experimental results with a femtosecond laser both at microscopic and macroscopic levels. We solved the Fokker-Planck equation using the CIP method for analyzing the interaction between a short-pulse-laser and plasma in the microscopic range. Here the Fokker-Planck equation is solved directly with an Eulerian grid in one-space and two-velocity space dimensions.

After the acceleration by the laser field, electrons are reflected back by a virtual cathode and contribute to the energy transport process. By this effect, the thermal flux quickly reached the Fourier law form. Such behavior is different from the previous result on non-local heat flow.

It is important to note that the classical transport theory (S-H theory) is quickly established within a very short time scale of the order of $\omega_p t = 50$.

Since the classical thermal conduction is realized so quickly, subsequent hydrodynamic calculation has been done in a purely classical manner and compared with the experiments. The simulations have shown that the damage diameter is much larger than the laser spot even in femtosecond-laser experiments. Thus the ablation depth dependence on laser fluence was correctly replicated only when the same definition of the fluence was used both in experiments and simulations.

ACKNOWLEDGMENTS

The authors would like to thank Dr. James Koga at Japan Atomic Research Institute and Professor Feng Xiao at Tokyo Institute of Technology for their careful reading of the manuscript and useful discussion.

[1] C. Momma, B.N. Chichkov, S. Nolte, F. von Alvensleben, A. Tunnermann, H. Welling, and B. Wellgehausen, Opt. Commun. **129**, 134 (1996).
[2] S. Nolte, C. Momma, H. Jacobs, A. Tunnermann, B.N. Chichkov, B. Wellegehausen, and H. Welling, J. Opt. Soc. Am. B **14**, 2716 (1997).
[3] T. Nakamura and T. Yabe, Comput. Phys. Commun. **120**, 122 (1999).
[4] T. Yabe and E. Takei, J. Phys. Soc. Jpn. **57**, 2598 (1988).
[5] T. Yabe and T. Aoki, Comput. Phys. Commun. **66**, 219 (1991).
[6] T. Yabe, F. Xiao, and T. Utsumi, J. Comput. Phys. **169**, 556 (2001).
[7] R. Tanaka, T. Nakamura, and T. Yabe, Comput. Phys. Commun. **126**, 232 (2000).
[8] T. Nakamura, R. Tanaka, T. Yabe, and K. Takizawa, J. Comput. Phys. **174**, 171 (2001).
[9] S. Brunner, E. Valeo, and J.A. Krommes, Phys. Plasmas **6**, 4504 (1999).
[10] S. Hain and P. Mulser, Phys. Rev. Lett. **86**, 1015 (2001).
[11] M.N. Rosenbluth, W.M. MacDonald, and D.L. Judd, Phys. Rev. **107**, 1 (1957).
[12] T. Utsumi, T. Kunugi, and T. Aoki, Comput. Phys. Commun. **101**, 9 (1997).
[13] A.R. Bell, R.G. Evans, and D.J. Nicholas, Phys. Rev. Lett. **46**, 243 (1981).
[14] L. Spitzer, Jr. and R. Harm, Phys. Rev. **89**, 977 (1953)
[15] T. Yabe and F. Xiao, Nucl. Eng. Des. **155**, 45 (1995).
[16] T. Yabe, in *Mathermatical Modeling of Weld Phenomena*, edited by H. Cerjak (University Press, Cambridge, 1998), Vol. 4, pp. 26–36.
[17] T. Yabe, Proc. SPIE **4157**, 1 (2000).
[18] K. Furusawa, K. Takahashi, H. Kumagai, K. Midorikawa, and M. Obara, Appl. Phys. A: Mater. Sci. Process. **69**, 359 (1999).
[19] Confirmed by the email of B.N. Chichkov.